

Numerical Investigation of Gust Load Alleviation for Wings with Passively Released FFWT

CHEN Tieren[1,2], ZENG Zhuqing[1,2], ZHAO Yue[1,2], HE Jiawen[1,2] & YANG Yong[1,2*]

[1] School of Aeronautics, NorthWestern Polytechnical University, Xi'an 710072, CHINA

[2] National Key Laboratory of Aircraft Configuration Design, Xi'an, 710072, CHINA

Abstract

To systematically investigate the gust response characteristics and gust load alleviation performance of high aspect ratio wings with passively released flared folding wingtips, a numerical investigation is conducted based on computational fluid dynamics. The flared folding wingtips is connected to the main wing via an elastically damping hinge, a rigid-body rotational dynamic model of the flared folding wingtips is established, and the interaction mechanism between wingtip deflection and unsteady aerodynamic loads is analyzed. For a high aspect ratio wing with a NACA0015 airfoil, numerical simulations under 1-cosine discrete gust disturbances are performed. The gust response and gust load alleviation performance of the fixed wingtip and flared folding wingtips configurations under different gust wavelengths are compared and analyzed, and the influences of key design parameters, including flared folding wingtips flare angle, hinge stiffness, damping, and flared folding wingtips moment of inertia, on the gust load alleviation effectiveness are further investigated.

Keywords: Folding Wingtips; High Aspect Ratio Wing; Gust Load Alleviation; Load Distribution

1. Introduction

Driven by the demand for improved fuel efficiency and reduced emissions in commercial aviation, High Aspect Ratio Wing (HARW) has become a core feature of next-generation large aircraft, with their unique aerodynamic benefits enabling significant induced drag reduction. To meet the requirements of airport gate, their wingtips are actively folded to shorten the wingspan. However, HARW aircraft experience significant higher wing gust loads than conventional aircraft. Current gust load alleviation (GLA) techniques can be divided into two main categories: active load control and passive load alleviation[1][2][3]. The passively released flared folding wingtips (FFWT) is an effective solution for GLA[4].

Most existing numerical studies on the FFWT use methods, like the vortex lattice method, panel methods and aerodynamic database approaches for aerodynamic load prediction. However, vortex lattice method and doublet lattice method cannot accurately capture complex unsteady flows[5]. Aerodynamic database methods use surrogate models built from steady CFD data across Mach numbers and angles of attack. The wing is split into rigid segments, and local aerodynamic coefficients are interpolated from each segment's local flow conditions[6]. These methods ignore unsteady effects like wake shedding and dynamic stall, leading to poor predictions of transient gust responses and load alleviation performance.

This study uses URANS simulations to analyze the gust response and GLA performance of an HARW with a passive FFWT. It covers three main parts:

(1) The discrete gust model is implemented. Gust velocities are added to the Navier-Stokes equations using the grid velocity method[16]. A rigid-body assumption is adopted for both the main

wing and FFWT. The main wing is fixed, while only the FFWT rotates about its hinge.
(2) Simulations of 1-cosine discrete gust are carried out for the HARW with a passive FFWT. The GLA performance of the FFWT is evaluated by comparing its gust response with that of the fixed FFWT. The study explores how gust wavelength affects the response and load reduction ability of the passive FFWT.
(3) A systematic parametric study is conducted to investigate four key FFWT parameters— flare angle,hinge stiffness, damping and moment of inertia.Their effects on aerodynamic loads and GLA performance are quantified

2. Numerical Model

2.1 Governing Equation

In this work, the field velocity method, proposed by Jones et al[16], is used to simulate gust effects. This method introduces the influence of the gust into the flow by adjusting the grid velocity in the specified region. For example, the continuity equation of the Navier-Stokes equations is written as:

$$\frac{d}{dt}\int_V \rho dV - \oint_S \rho(\vec{v} - \vec{v}_B - \vec{v}_{grid})d\vec{S} = 0 \tag{1}$$

$\vec{v}_{grid}$ denotes the velocity vector of the grid.For a steady freestream, relative motion means grid motion produces the same aerodynamic effect as a stationary domain with an incoming flow of opposite speed. If the positive coordinate coincides with the gust direction, the gust velocity is added to the grid velocity.

2.2 Dynamic Governing Equation of the Flared FFWT

FFWT is modeled as a rigid body, and connected to the main wing via an elastic damping hinge (EDH), with the hinge stiffness denoted as K_M , damping as D_M , and the FFWT moment of inertia about the hinge axis as I_M . Let η 、 $\dot{\eta}$ and $\ddot{\eta}$ represent the hinge deflection angle, angular rate, and angular acceleration of the FFWT about the hinge axis. The corresponding governing dynamic equation is given by Equation (2):

$$M_T = K_M \bullet \eta + D_M \bullet \dot{\eta} + I_M \ddot{\eta} \tag{2}$$

where M_T denotes aerodynamic hinge moment on the FFWT about the hinge axis.

2.3 Geometric Model

The HARW uses a NACA0015 airfoil with no twist. The wing is defined with an aspect ratio of $\lambda = 17.9$ and a reference chord length of $c = 1.0m$. Figure 1 shows the half-span geometric model.

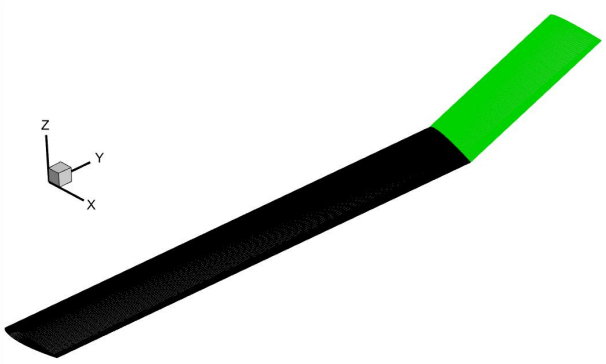


Figure 1 – Geometry of the HARW

The FFWT accounts for 25% of the half-span with a flare angle $\Lambda = 10^\circ$. Detailed geometric parameters of the FFWT are listed in Table 1. S_f denotes the area of the FFWT, M represents the

mass of the FFWT, while K_M and C_M correspond to the hinge stiffness and damping.

Table 1 - FFWT design parameters for HARW

S_f, m^2	2.225
M, kg	174
$\Lambda, ^\circ$	10
$K_M, N \bullet M / rad$	0.2
$C_M, N \bullet M \bullet s / rad$	0.02

3. Gust Load Alleviation Analysis of the FFWT

3.1 Computational Cases

To investigate the influence of gust wavelength on the gust response and GLA performance of the FFWT, a series of numerical simulations are performed at a freestream velocity $V_\infty = 18 m/s$. The discrete gust follows the standard 1-cosine profile, with a gust velocity $V_{gust} = 1.57 m/s$. The gust wavelengths are set to 12, 15, 30, 45, 60, and 120 reference chord lengths. The 12-chord wavelength case is denoted as $\lambda_g = 12.0c$ for brevity.

3.2 Gust Responses

Figure 2 and 3 present the lift responses of the FIX and the FFWT configuration under gusts of different wavelengths. Figure 4 compares peak load with different gust wavelength for both configurations. Figures 5 show the FFWT hinge deflection responses with different gust wavelength. Table 2 lists the peak load and load reduction rates.

From figure 4, peak load for the FIX configuration rises steadily with gust wavelength, with its growth slowing until gust load stabilizes. For the FFWT, peak load decreases when gust wavelength exceeds $\lambda_g = 45.0c$. From table 2, a load reduction rate $\Delta C_L{}^{FFWT} = -14.82\%$ is achieved at a gust wavelength $\lambda_g = 120.0c$. The rise in maximum FFWT hinge deflection also weakens at larger gust wavelengths.

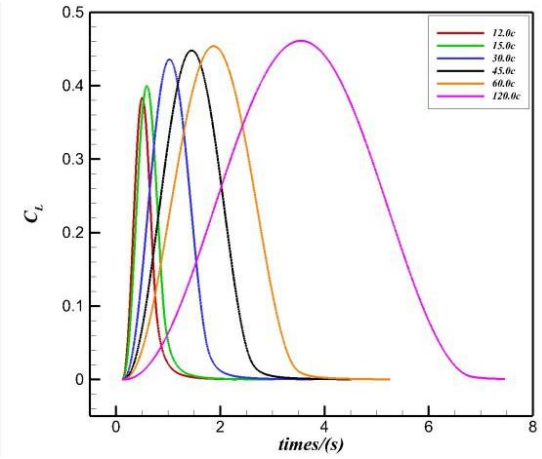


Figure 2 – The responses of lift for the FIX

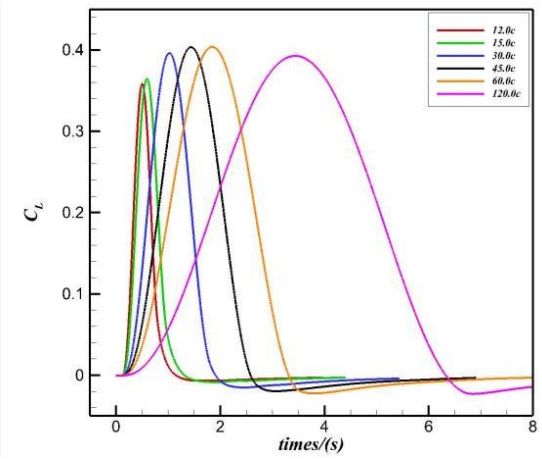


Figure 3 – The responses of lift for the FFWT

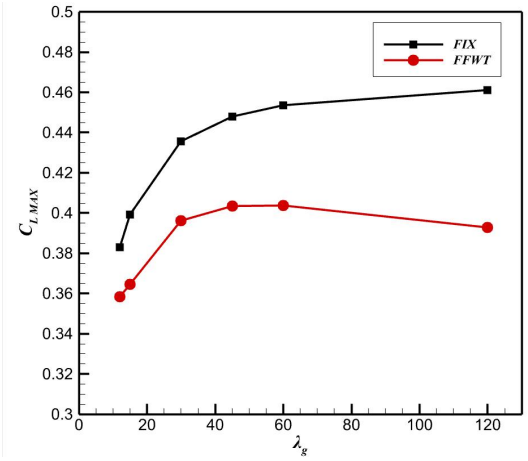


Figure 4 – Peak load with gust wavelength

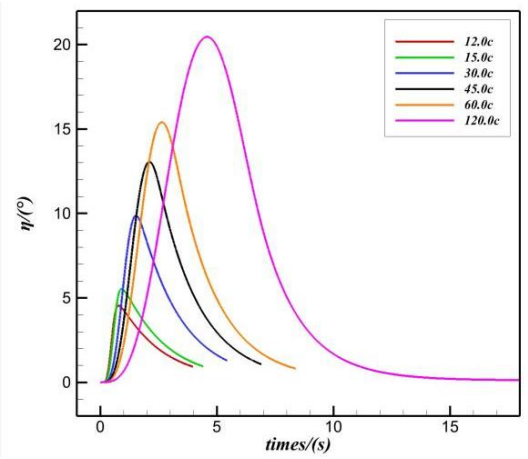


Figure 5 – The FFWT hinge deflection angle histories

3.3 GLA Performance

Figure 6 and 7 present the wing boot bending moment (WRBM) responses of the FIX and FFWT configuration under gusts of different wavelengths. The response of WRBM follows the same trend as that of lift, so no further responses of WRBM are presented later.

Table 3 lists peak WRBM and the load reduction rates across all tested wavelengths. For the FFWT, WRBM peaks at a wavelength $\lambda_g = 30.0c$. The WRBM reduction $\Delta WRBM^{FFWT} = -25.77\%$ occurs at $\lambda_g = 120.0c$.

Figures 8 to 11 compare the spanwise distributions of normal force, bending moment and torsional moment alleviation at peak load for both configurations. Figure 11 presents the peak lift and WRBM alleviation with different gust wavelength.

Under gusts, loads on the FIX configuration rise steadily with gust wavelength. By contrast, normal force on the FFWT decreases gradually. For $\lambda_g \le 30.0c$, the FFWT bending moment rises with wavelength at inboard sections near the wing root, while the growth slows toward the wingtip hinge. At more outboard stations, bending moment declines as wavelength increases. For $\lambda_g \ge 30.0c$, bending moment falls continuously with wavelength, with a more obvious reduction near the wing root.

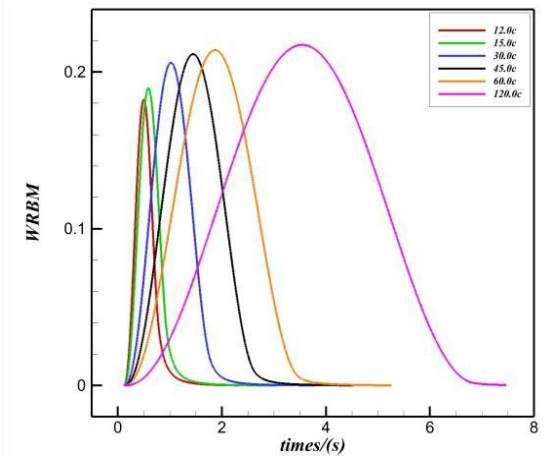


Figure 6 – responses of WRBM for the FIX

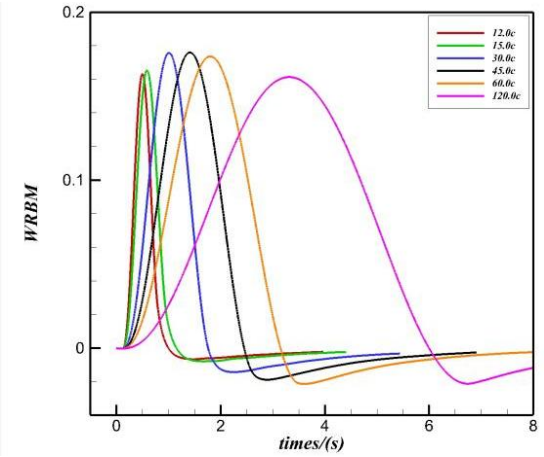


Figure 7 – responses of WRBM for the FFWT

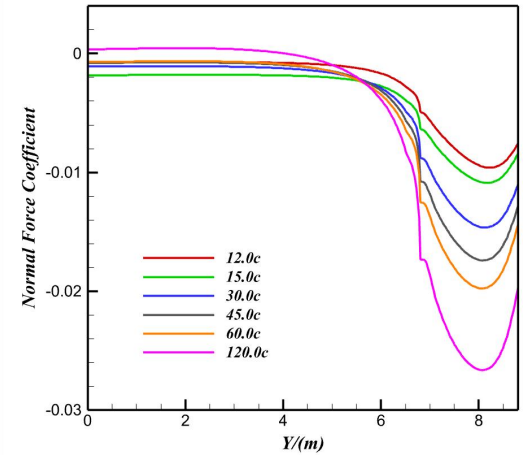


Figure 8 – Normal force reduction along the span

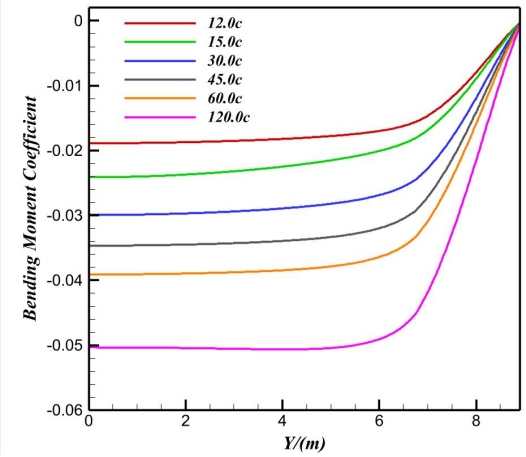


Figure 9 – Bending moment reduction along the span

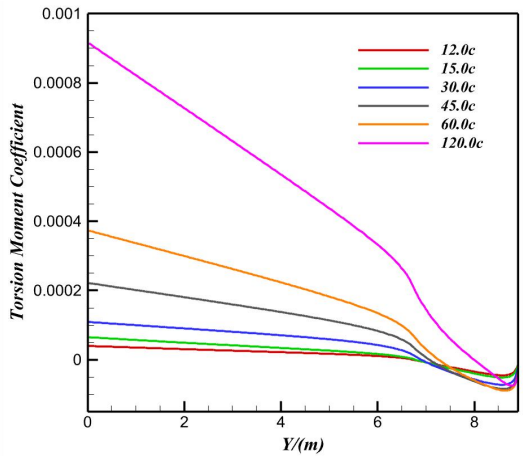


Figure 10 – Torsion moment reduction along the span

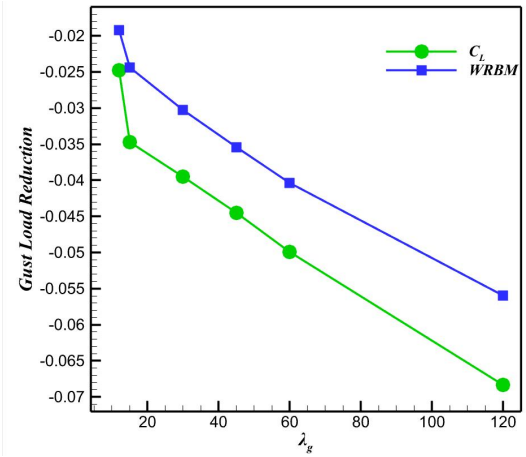


Figure 11 – Gust load reduction with different gust wavelength

Table 2. Comparison of gust load with different gust wavelength

λ_g	C_L^{FIX}	C_L^{FFWT}	ΔC_L^{FFWT}	$WRBM^{FIX}$	$WRBM^{FFWT}$	$\Delta WRBM^{FFWT}$
12.0c	0.3830	0.3583	-6.45%	0.1824	0.1632	-10.53%
15.0c	0.3993	0.3646	-8.69%	0.1897	0.1653	-12.86 %
30.0c	0.4356	0.3961	-9.07%	0.2059	0.1757	-14.67 %
45.0c	0.4479	0.4033	-9.96%	0.2113	0.1760	-16.71 %
60.0c	0.4536	0.4037	-11.00%	0.2140	0.1736	-18.88 %
120.0c	0.4610	0.3927	-14.82%	0.2173	0.1613	-25.77 %

Notably, the FFWT does not produces reduction in wing root torsion moment. Although this moment rises only slightly, its growth rate along the span is higher for the FFWT than for the FIX configuration. Since the rise in root torsion moment is much smaller than that of WRBM, further results for torsion moment are not shown below.

4. Influence of FFWT Parameters on GLA Performance

The FFWT is connected to the main wing via an EDH. As shown earlier, the passively FFWT produces effective GLA for the wing under gusts. Numerical simulations are performed for standard 1-cosine discrete gusts, with four key design parameters varied: hinge flare angle, stiffness, damping and inertia moment of FFWT. Their effects on GLA performance are analysed systematically.

4.1 Influence of Hinge Flare Angle

All simulations in this section are conducted at a gust wavelength $\lambda_g = 45.0c$. The flare angle, denoted as Λ , is defined as the angle between the hinge axis and the freestream flow direction. A positive flare angle $\Lambda > 0$ is defined as the hinge axis rotating outboard relative to the freestream direction, as illustrated in Figure 15.

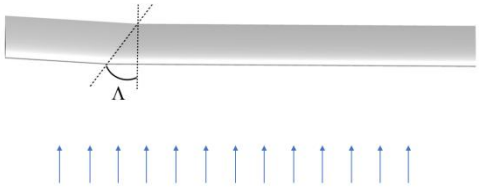


Figure 12. The flare angle definition for the FFWT

The FFWT hinge deflection angle is denoted as η , with upward deflection defined as $\eta > 0$. The variation in the local angle of attack of the FFWT can be expressed by Equation (3):

$$\Delta\alpha_{FFWT} = -\tan^{-1}(\tan\eta \bullet \sin\Lambda) \tag{3}$$

As shown in Equation (3), for $\Lambda > 0$, upward deflection of the FFWT reduces the local angle of attack. Accordingly, the FFWT hinge flare angles are set to $\Lambda = 5^\circ$, 10° , 15° , 20° , 25° , 30° in this study.

Figures 13 to 14 show gust responses and FFWT hinge deflection. Table 5 lists the peak load and load reduction levels.Figures 15–18 show the spanwise load alleviation distributions at peak load, while Figure 18 presents the overall peak lift and WRBM alleviation across different flare angles.

Results show that the FFWT moves the peak load to an earlier time instant. A larger flare angle brings an earlier and lower peak load, which improves GLA performance. However, the incremental reduction in peak load gradually decreases. Increase of the flare angle also advances the time of maximum hinge deflection. WRBM exhibits a similar trend to lift, with even more significant reduction. After the gust passes, the FFWT returns to its original position at all tested flare angles; larger flare angles enable faster recovery.

The sectional normal force on the FFWT is lower than that on the FIX configuration, and the load reduction becomes more pronounced near the wingtip. Normal force reduction rises with flare angle. Sectional bending moment also decreases as flare angle increases, though the reduction rate gradually slows. Once the flare angle exceeds a critical value, sectional gust loads gradually level off.

Table 3. Comparison of the gust load with flare angle

	C_L	ΔC_L	*WRBM*	Δ*WRBM*	C_{LMAX} $\eta/(^\circ)$	η_{MAX} $\eta/(^\circ)$
FIX	0.4479	/	0.2114	/	/	/
$\Lambda = 5^\circ$	0.4133	-7.72%	0.1837	-13.10%	10.448	15.749
$\Lambda = 10^\circ$	0.4034	-9.94%	0.1760	-16.75%	8.640	13.059
$\Lambda = 15^\circ$	0.3956	-11.68%	0.1701	-19.54%	7.818	11.302
$\Lambda = 20^\circ$	0.3895	-13.04%	0.1656	-21.67%	7.071	9.867
$\Lambda = 25^\circ$	0.3850	-14.04%	0.1622	-23.27%	6.386	8.723
$\Lambda = 30^\circ$	0.3811	-14.92%	0.1594	-24.60%	5.806	7.794

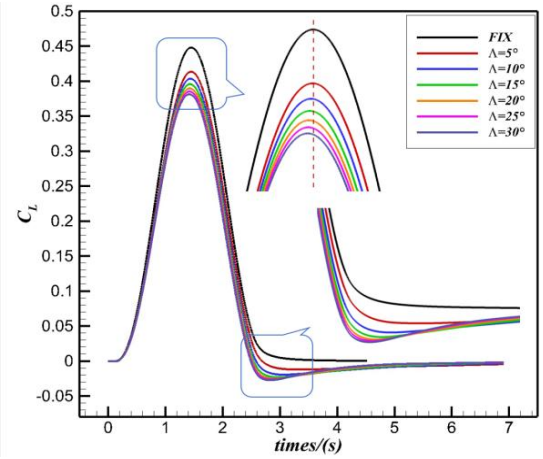


Figure 13. The responses of lift

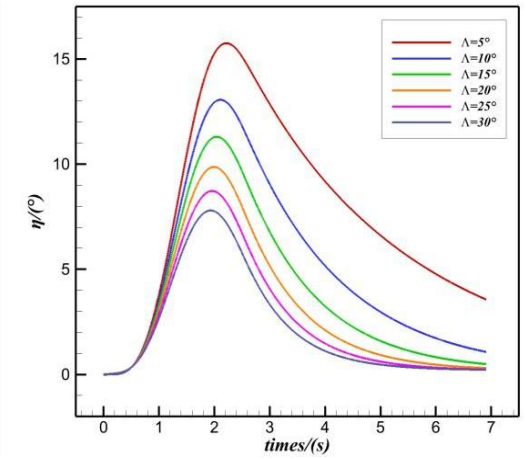


Figure 14 – The responses of hinge deflection angle

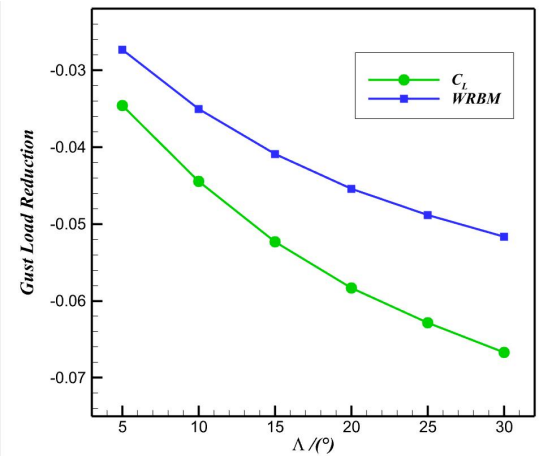


Figure 15. Gust load reduction with flare angle

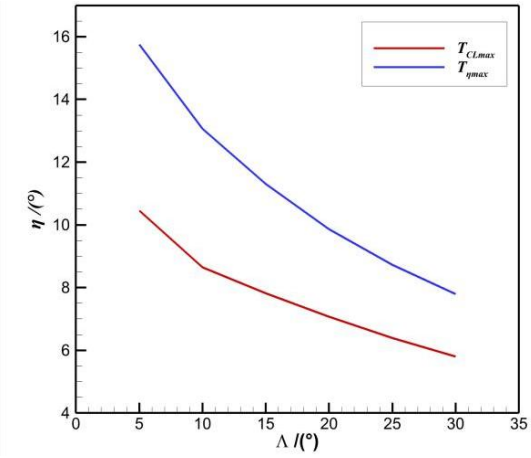


Figure 16. Peak hinge deflection angle with flare angle

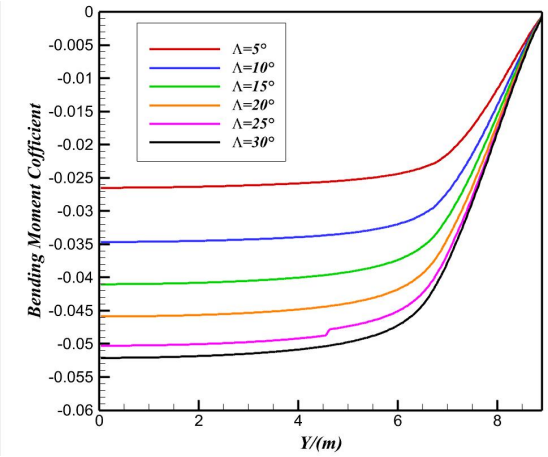


Figure 17 – Bending moment reduction along the span

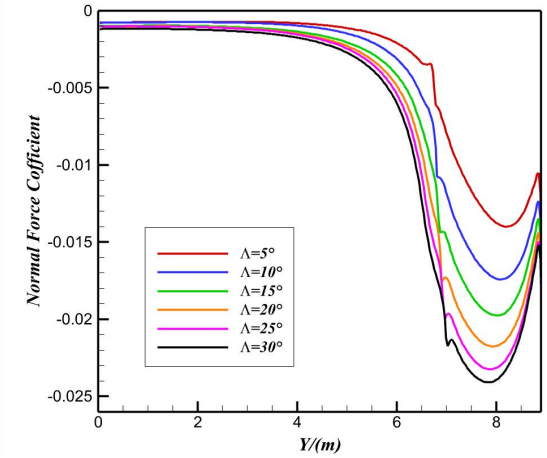


Figure 18 – Normal force reduction along the span

4.2 Influence of Hinge Rotational Stiffness

All simulations in this section are conducted with a FFWT flare angle $\Lambda = 10^{\circ}$. The hinge stiffness dominates the maximum deflection angle of the FFWT, thereby influencing the GLA performance. To investigate the correlation between hinge stiffness and aerodynamic parameters, a non-dimensional hinge stiffness is introduced, as defined in Equation (4):

$$K_d = \frac{K_M}{qS_f b_f} \tag{4}$$

where K_M is the hinge stiffness, q is the freestream dynamic pressure, S_f is the area of the FFWT, and b_f is the span length of the FFWT segment.

Figures 19 to 20 show lift and FFWT hinge deflection. Figures 21 – 23 show the spanwise load alleviation distributions at peak load, while Figure 21 presents the overall peak lift and WRBM alleviation across different hinge stiffness. Since WRBM follows the same trend as lift, its results are not repeated here for brevity.

Lift response correlates closely with FFWT hinge deflection. A stiffer hinge reduces deflection, which weakens GLA. As hinge stiffness decreases, GLA performance gradually converges to a steady limit. At sufficiently high stiffness, the FFWT deflects only slightly. The sectional normal force decreases slightly, yet the bending moment shows little to no reduction, or even increases, compared with the FIX configuration.

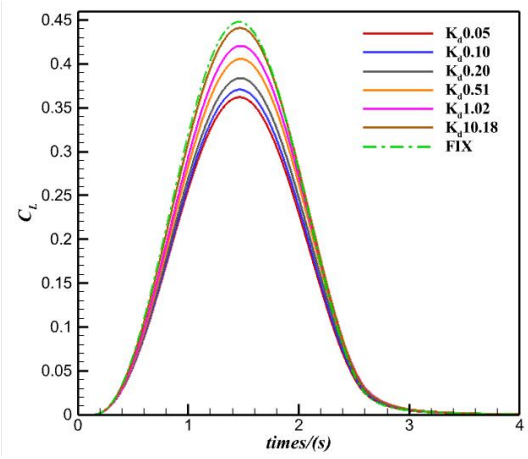


Figure 19. The responses of lift

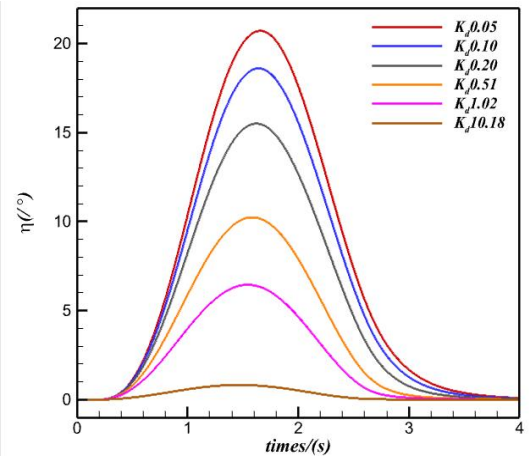


Figure 20. The responses of hinge deflection angle

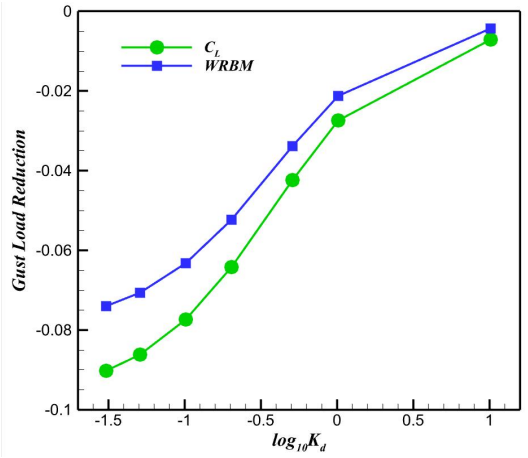


Figure 21 – Gust load reduction with different stiffness

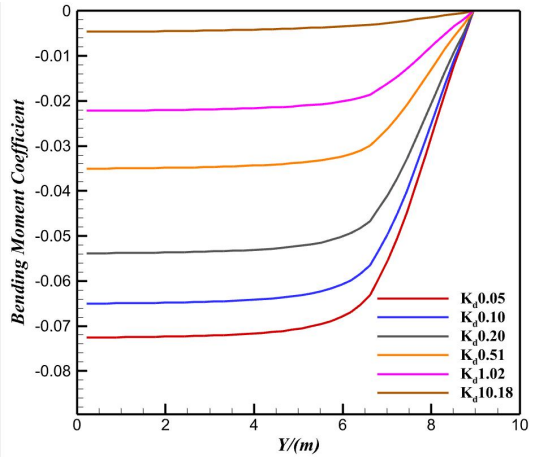


Figure 22 – Bending moment reduction along the span

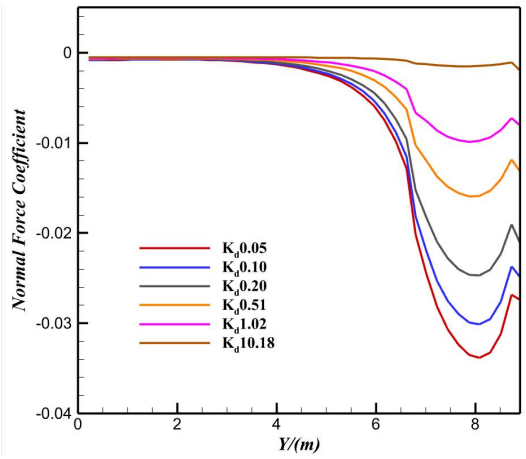


Figure 23 - Normal force reduction along the span

Table 4. Comparison of the GLA with hinge stiffness

K_d	C_L	ΔC_L	$WRBM$	$\Delta WRBM$
FIX	0.4479	/	0.2114	/
0.05	0.36181	-19.22%	0.14084	-33.38%
0.10	0.37054	-17.27%	0.14815	-29.92%
0.20	0.383646	-14.35%	0.15918	-24.70%
0.51	0.405523	-9.46%	0.1776	-15.99%
1.02	0.420483	-6.12%	0.19015	-10.05%
10.18	0.440826	-1.58%	0.20717	-2.00%

4.3 Influence of Hinge Rotational Damping

All simulations in this section adopt for hinge stiffness $K_d = 0.1$ and FFWT moment of inertia about the hinge axis $I_d = 2.36$. The conventional damping ratio $\zeta = D_M / 2\sqrt{I_M K_M}$ is not suitable for this system, since aerodynamic damping is tightly coupled with deflection and aerodynamic loads under gusts. This work therefore aims to quantify how hinge damping influences gust response and GLA performance.The non-dimensional rotational damping of the FFWT hinge is defined in Equation (5):

$$D_d = \frac{D_M V_\infty}{q S_f b_f^2} \tag{5}$$

where D_d denotes the non-dimensional hinge damping.

Figures 24 to 25 show lift and FFWT hinge deflection. Figures 26 – 28 show the spanwise load alleviation distributions at peak load, while Figure 28 presents the overall peak lift and WRBM alleviation across different hinge damping.

At low hinge damping, aerodynamic damping dominates in the FFWT system, so hinge damping has negligible impact on system responses. It exerts a clear influence on the FFWT only when it exceeds the aerodynamic damping of the system.

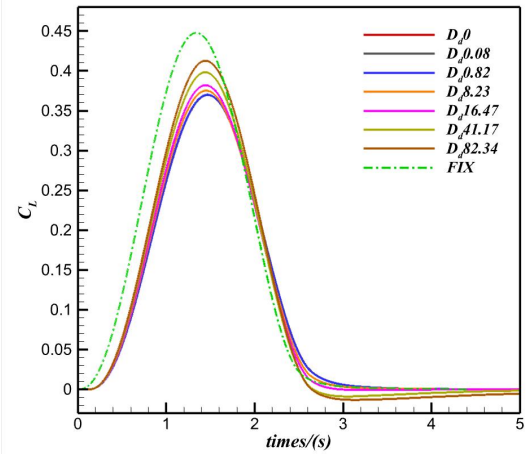


Figure 24. The responses of lift

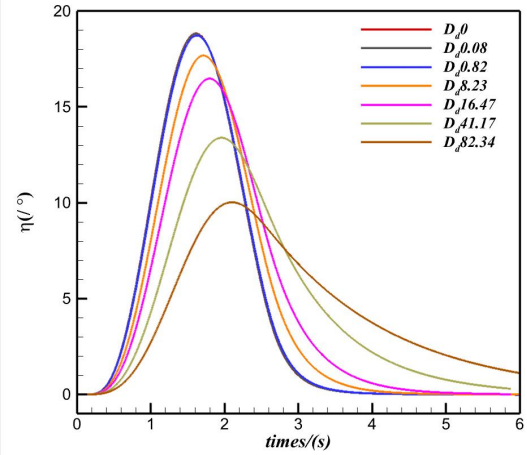


Figure 25. The responses of hinge deflection angle

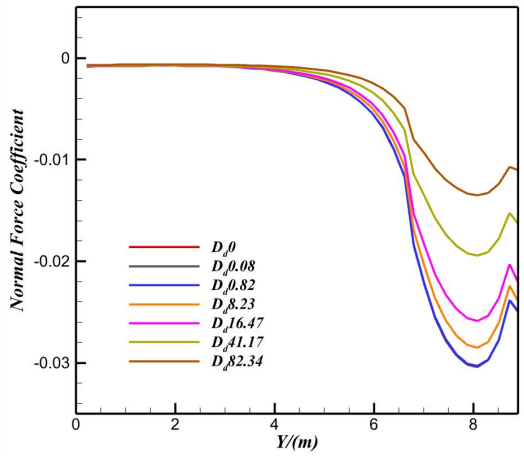


Figure 26 – Normal force reduction along the span

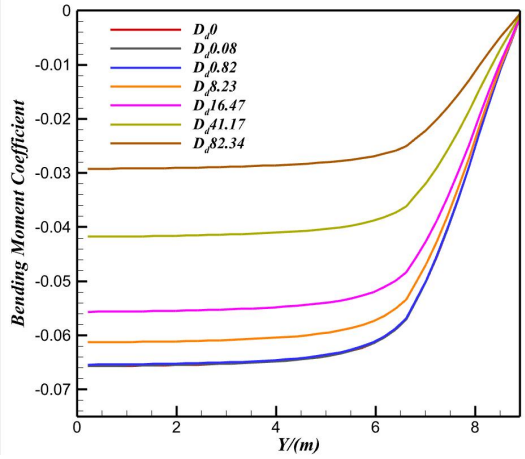


Figure 27 – Bending moment reduction along the span

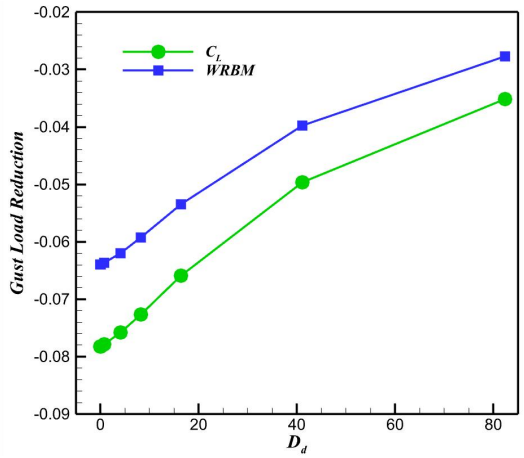


Figure 28. Gust load reduction with different damping

Table 5. Comparison of the GLA with hinge damping

C_d	C_L	ΔC_L	$WRBM$	$\Delta WRBM$
FIX	0.4479	/	0.2114	/
0.00	0.3696	-17.48%	0.1474	-30.27%
0.08	0.3697	-17.47%	0.1474	-30.26%
0.82	0.3700	-17.39%	0.1477	-30.12%
8.23	0.3752	-16.23%	0.1521	-28.04%
16.47	0.3820	-14.71%	0.1579	-25.29%
41.17	0.3983	-11.09%	0.1716	-18.82%
82.34	0.4128	-7.84%	0.1837	-13.08%

4.4 Influence of FFWT Mass Moment of Inertia

All simulations in this section are conducted with hinge stiffness $K_d = 0.20$. The non-dimensional FFWT moment of inertia is defined in Equation (6):

$$I_d = \frac{I_M V_\infty^2}{\pi q S_f^2 b_f} \tag{6}$$

where I_d is the non-dimensional FFWT moment of inertia about the hinge axis.

Figures 29 to 32 show lift and FFWT hinge deflection. Figures 33 to 38 show the spanwise load alleviation distributions at peak load, while Figure 37 presents the overall peak lift and WRBM alleviation across different FFWT Moment of Inertia.For Figure 37, solid lines represent the load alleviation at $\zeta = 1.5$, while dashed lines denote the load alleviation at $D_d = 0.08$.

For a given damping ratio, GLA performance changes monotonically with FFWT moment of inertia. A larger moment of inertia degrades GLA performance, while performance remains nearly unchanged at low inertia. With hinge damping held constant, three distinct GLA characteristics appear with different FFWT moment of inertia:

(1) Aerodynamic dominated overdamped behaviour: FFWT deflection is driven primarily by aerodynamic loads for GLA, and the system operates in the overdamped state.

(2) Mixed aerodynamic–inertial critically damped behaviour: Aerodynamic loads and inertial forces jointly govern FFWT motion, and the system operates in the critically damped state.

(3) Inertia dominated underdamped behaviour: Inertial forces control FFWT motion, and the system

operates in the underdamped state.

The system reaches the exact critical damping state at a FFWT moment of inertia $I_d = 94.36$. The damping ratio is calculated as $\zeta = 7.9 \times 10^{-3} \ll 1.0$. This reveals that aerodynamic damping dominates the total damping of the FFWT system. Figure 38 further confirms this trend. Structural damping dissipates little energy, while aerodynamic damping accounts for most of the system's energy loss.

As shown in Figures 33 and 34, the phase-lagged FFWT response enhances the normal force alleviation performance of the main wing, leading to superior load reduction at the wing root.From table 6, the optimal GLA performance occurs at a FFWT moment of inertia $I_d = 235.90$ and the load reduction are $\Delta WRBM = -30.07\%$ and $\Delta C_L = -17.39\%$.

Table 6. Comparison of the GLA with FFWT moment of inertia with $D_d = 0.08$

I_d	C_L	ΔC_L	$WRBM$	$\Delta WRBM$
FIX	0.4479	/	0.2114	/
148.22	0.38081	-14.98%	0.15684	-25.81%
296.44	0.37796	-15.62%	0.15443	-26.95%
592.88	0.37192	-16.96%	0.14929	-29.38%
741.09	0.37003	-17.39%	0.14784	-30.07%
1482.19	0.37266	-16.80%	0.15145	-28.36%
7410.95	0.41346	-7.69%	0.18488	-12.54%
14821.90	0.42652	-4.77%	0.19538	-7.58%

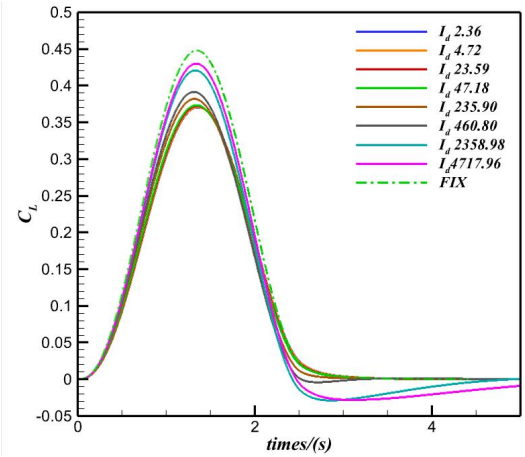


Figure 29. The responses of lift with $\zeta = 1.5$

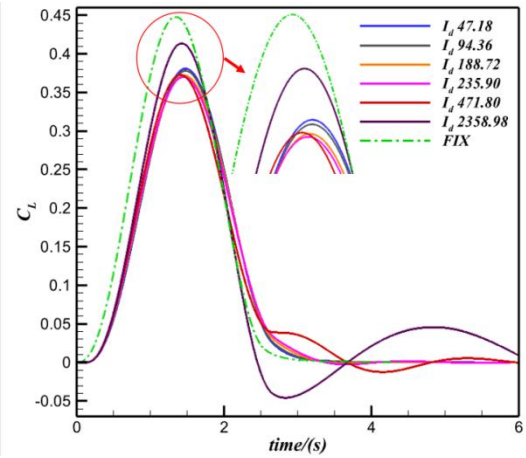


Figure 30. The responses of lift with $D_d = 0.08$

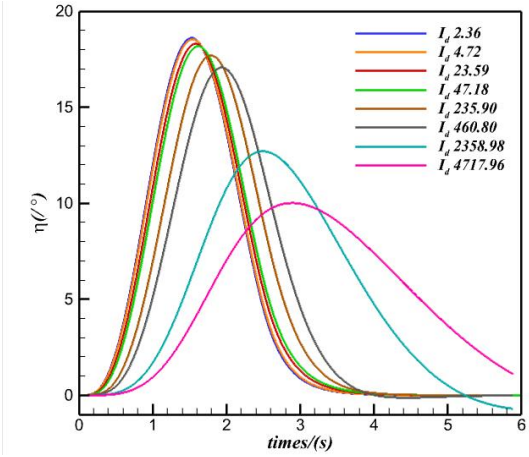


Figure 31. The responses of hinge deflection angle with $\zeta = 1.5$

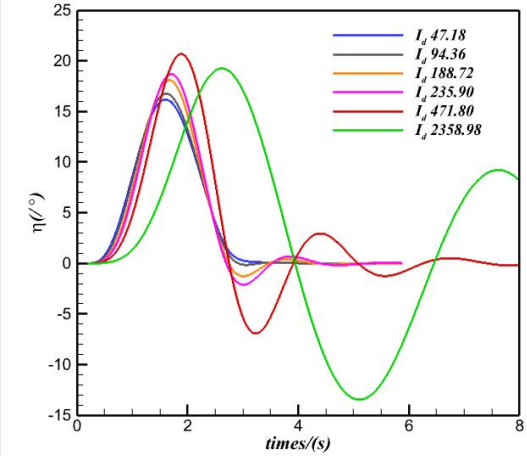


Figure 32. The responses of hinge deflection angle with $D_d = 0.08$

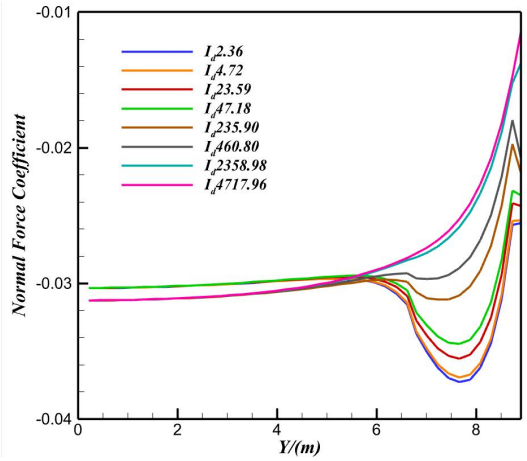


Figure 33 – Normal force reduction along the span with $\zeta = 1.5$

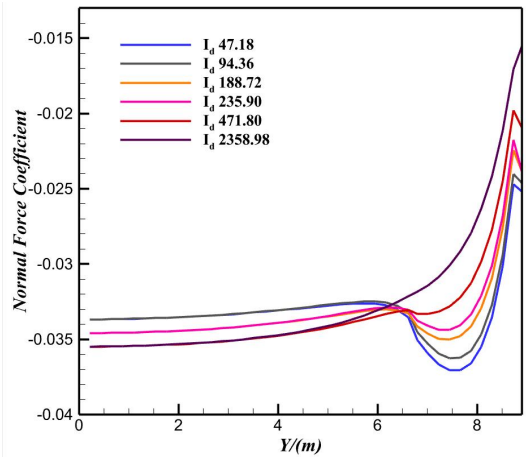


Figure 34 – Normal force reduction along the span with $D_d = 0.08$

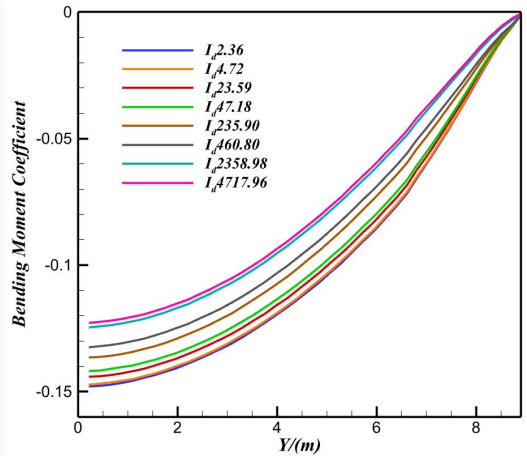


Figure 35 – Bending moment reduction along the span with $\zeta = 1.5$

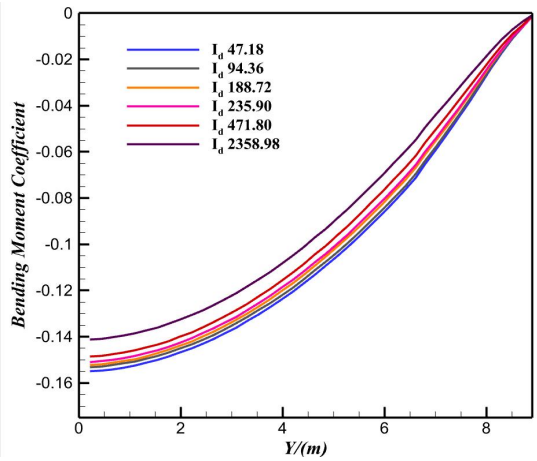


Figure 36 – Bending moment reduction along the span with $D_d = 0.08$

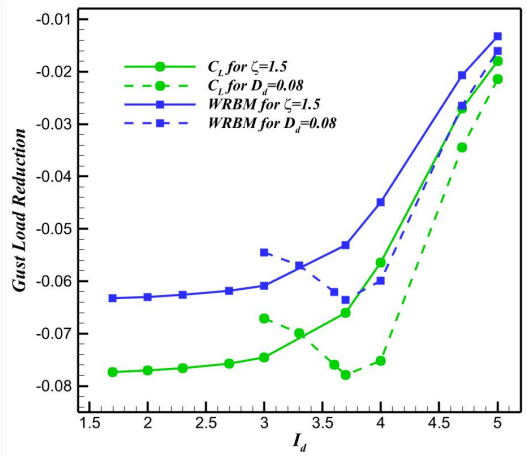


Figure 37. Gust load reduction with different FFWT moment of inertia

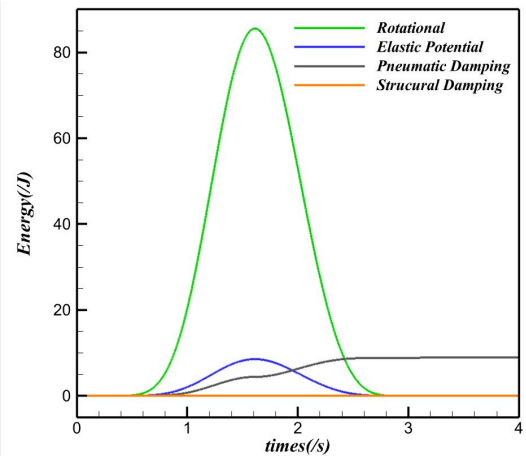


Figure 38. The responses of the FFWT system energy with $D_d = 0.08$ $I_d = 94.36$

5. Conclusions

In this work, a rigid-body rotational dynamic model for the FFWT equipped with an EDH is established. Numerical simulations of gust responses to 1-cosine discrete gusts are carried out for a HARW with NACA0015 airfoil sections. Based on the above numerical results and systematic

analysis, the main conclusions are summarized as follows:

(1) Over the investigated gust wavelength range from 12c to 120c, peak loads of the FIX configuration rise monotonically with gust wavelength and gradually approach a nearly constant value. By contrast, peak load of the passively deployed FFWT configuration first increases and then decreases, reaching its maximum at a gust wavelength $\lambda_g = 45.0c$. A longer gust wavelength enables larger deflection of the FFWT, leading to steady improvement in GLA performance. At a gust wavelength $\lambda_g = 120.0c$, peak loads are reduced by 14.82% for lift and 22.77% for WRBM.

(2) For hinge flare angles ranging from 5° to 30°, peak loads decrease as the flare angle increases, accompanied by continuous improvement in GLA performance, which eventually converges asymptotically to a limiting value.

(3) As hinge stiffness approaches zero, GLA performance converges to its theoretical upper limit. When stiffness tends to infinity, the load characteristics match those of the FIX configuration. The most significant variation in peak load occurs at non-dimensional hinge stiffness between 0.1 and 1.0.

(4) Aerodynamic damping dominates the total damping of the FFWT system, whereas structural hinge damping has a negligible influence on system responses. Structural damping contributes substantially to energy dissipation only when it is comparable to aerodynamic damping. For this reason, the conventional damping ratio is not suitable for describing the damping characteristics of the FFWT system.

(5) Changing FFWT moment of inertia results in three distinct GLA response behaviors: aerodynamic dominated overdamped behavior, mixed aerodynamic inertial critically damped behavior, and inertia dominated underdamped behavior. The non-dimensional FFWT moment of inertia of 47.18 is the critical value, at which the system operates exactly under critical damping. The optimal GLA performance is obtained at a non-dimensional inertia moment of 235.90, with peak load reduced by 17.39% for lift and 30.07% for WRBM.

6. Contact Author Email Address

YANG Yong: yyang@nwpu.edu.cn

7. Copyright Statement

The authors confirm that they, and/or their company or organization, hold copyright on all of the original material included in this paper. The authors also confirm that they have obtained permission, from the copyright holder of any third party material included in this paper, to publish it as part of their paper. The authors confirm that they give permission, or have obtained permission from the copyright holder of this paper, for the publication and distribution of this paper as part of the ICAS proceedings or as individual off-prints from the proceedings.

References

[1] De Souza, A. R., Vuillemin, P., Poussot-Vassal, C., et al. Gust load alleviation using reduced-order aeroelastic m odels and observer-based robust control. *Journal of Guidance, Control, and Dynamics*. 2023, 46(5): 949-957. DO I:10.2514/1.G007153.

[2] Zhao, Y. H., Yue, C. Y., Hu, H. Y. Gust load alleviation on a large transport airplane. *Journal of Aircraft*. 2016, 5 3(6): 1932-1946. DOI:10.2514/1.C033713.

[3] Zhang, S. S., Qiu, Y. H., Sun, J. S., et al. Gust load alleviation control strategies for large civil aircraft through wi ng camber technology. *Actuators*. 2024, 13(6). DOI:10.3390/act13060229.

[4] Castrichini, A., Siddaramaiah, V. H., Calderon, D. E., et al. Nonlinear folding wing tips for gust loads alleviation. In: *56th AIAA/ASME/ASCE/AHS/ASC Structures, Structural Dynamics and Materials Conference / 33rd Wind En ergy Symposium*. 2016: 1391-1399.

[5] Cheung, R. C. M., Wales, C., Rezgui, D., et al. Modelling of folding wing-tip devices for gust loads alleviation. In: *AIAA/ASCE/AHS/ASC Structures, Structural Dynamics, and Materials Conference*. 2018: 904-915.

[6] Sanghi, D., Cesnik, C. E. S., Riso, C. Roll maneuverability of transonic high-aspect-ratio-wing aircraft with flared folding wingtips. *Journal of Aircraft*. 2024, 61(3): 915-938. DOI:10.2514/1.C037470.

[7] Castrichini, A., Siddaramaiah, V. H., Calderon, D. E., et al. Preliminary investigation of use of flexible folding wi ng tips for static and dynamic load alleviation. *The Aeronautical Journal*. 2017, 121(1235): 73-94. DOI:10.1017/a er.2016.108.

[8] Wilson, T., Castrichini, A., Azabal, A., et al. Aeroelastic behaviour of hinged wing tips. In: *17th International For um on Aeroelasticity and Structural Dynamics, IFASD 2017*. 2017.

[9] Yang, C., Qiu, Q. S., Zhou, Y. T., et al. A review of aircraft gust response alleviation technology. *Acta Aeronautic a et Astronautica Sinica*. 2022, 43(10): 208-248.

[10] Cheung, R. C., Castrichini, A., Rezgui, D., Cooper, J. E., Wilson, T. Testing of wing-tip spring device for gust l oads alleviation. In: *58th AIAA/ASCE/AHS/ASC Structures, Structural Dynamics, and Materials Conference*. 2017. DOI:10.2514/6.2017-0630.

[11] Cheung, R. C. M., Rezgui, D., Cooper, J. E., Wilson, T. Testing of folding wingtip for gust load alleviation of fl exible high-aspect-ratio wing. *Journal of Aircraft*. 2020, 57(5): 876-888.

[12] Balatti, D., Khodaparast, H. H., Friswell, M. I., et al. Improving gust load alleviation performance of hinge wing tip using validated aeroelastic models. *SSRN*. 2022.

[13] Balatti, D., Khodaparast, H. H., Friswell, M. I., et al. Experimental and numerical investigation of an aircraft wi ng with hinged wingtip for gust load alleviation. *Journal of Fluids and Structures*. 2023, 119. DOI:10.1016/j.jflui dstructs.2023.103892.

[14] Wales, C., Jones, D., Gaitonde, A. Prescribed velocity method for simulation of aerofoil gust responses. *Journal of Aircraft*. 2015, 52(1): 64-76.

[15] Xu, X. P., Zhang, Y. J. Research on wing gust response based on CFD method. *Aircraft Design*. 2011, 31(2): 20 -24. DOI:10.19555/j.cnki.1673-4599.2011.02.005.

[16] Bisplinghoff, R. L., Ashley, H., Halfman, R. L. *Aeroelasticity*. New York: Dover Publications; 1996. pp. 45–52.